

# Analysis of differential infrared thermography for boundary layer transition detection

A. D. Gardner<sup>1</sup>  · C. Eder<sup>2</sup> · C. C. Wolf<sup>1</sup> · M. Raffel<sup>1</sup>

Received: 17 February 2017 / Revised: 14 June 2017 / Accepted: 17 July 2017 / Published online: 18 August 2017  
© Springer-Verlag GmbH Germany 2017

**Abstract** This paper presents an analysis of the differential infrared thermography (DIT) technique, a contactless method of measuring the unsteady movement of the boundary layer transition position on an unprepared surface. DIT has been shown to measure boundary layer transition positions which correlate well with those from other measurement methods. In this paper unsteady aerodynamics from a 2D URANS solution are used and the resulting wall temperatures computed. It is shown that the peak of the temperature difference signal correlates well with the boundary layer transition position, but that the start and end of boundary layer transition cannot be extracted. A small systematic time-lag cannot be reduced by using different surface materials, but the signal strength can be improved by reducing the heat capacity and heat transfer of the surface layer, for example by using a thin plastic coating. Reducing the image time separation used to produce the difference images reduces the time-lag and also the signal level, thus the optimum is when the signal to noise ratio is at the minimum which can be evaluated.

## List of symbols

$\alpha$	Instantaneous angle of attack (°)
$\alpha_0$	Mean angle of attack (°)
$\alpha_1$	Pitching amplitude (°)
$a_d$	Thermal diffusivity (m <sup>2</sup> /s)
$c$	Airfoil chord length (m)
$C_f$	Skin friction coefficient
$C_p$	Pressure coefficient
$\sigma C_p$	Standard deviation in $C_p$
$C$	Specific heat capacity (J/kg/K)
$\Delta T$	Temperature difference between two times (K)
$\epsilon$	Emissivity
$f$	Pitching frequency (Hz)
$f_i$	Image time separation (acquisition) frequency (Hz)
$f_0$	Focal length (m)
$f \times t$	Normalised period time
$H_L$	Lamp heat flux (W/m <sup>2</sup> )
$k_v$	Thermal conductivity vertically (W/m/K)
$k_h$	Thermal conductivity horizontally (W/m/K)
$M$	Mach number
$N$	Boundary value for the transition code
$\dot{q}$	Heat flux (W)
$\rho$	density (kg/m <sup>3</sup> )
$Re$	Reynolds number
$t$	Time (s)
$T$	Wall temperature (K)
$T_r$	Flow recovery temperature (K)
$Tu$	Freestream turbulence level
$v$	Local flow velocity (m/s)
$x$	Coordinate in the flow direction (m)
$y$	Coordinate in breadth (m)
$z$	Coordinate in depth (vertical) (m)

✉ A. D. Gardner  
Tony.Gardner@dlr.de

C. C. Wolf  
Christian.Wolf@dlr.de

M. Raffel  
Markus.Raffel@dlr.de

<sup>1</sup> German Aerospace Center (DLR), Institute of Aerodynamics and Flow Technology, Bunsenstrasse 10, 37073 Göttingen, Germany

<sup>2</sup> Department of Mechanical Engineering, Bundeswehr University Munich, 85577 Neubiberg, Germany

## 1 Introduction

Unsteady boundary layer transition is an important phenomenon, having an effect on the efficiency and stall point of helicopter main rotor blades (Heister 2013; Richter and Schülein 2014; Raffel et al. 2011), Wind turbines (Du and Selig 2000; Langtry et al. 2006; Lanzafame et al. 2013) and propellers (Schülein 2014). Many of the classical methods of detecting steady boundary layer transition, including china clay/sublimation (Richards and Burstall 1945; Velkoff et al. 1971) do not work for unsteady flows. Other methods, including hot-film anemometry (Schultz and Jones 1973), microphones (Døssing 2008) or the  $\sigma C_p$  method of pressure analysis (Gardner and Richter 2015) require the installation of finely discretised sensor arrays and significant data analysis. Hot-wire or Pitot boundary layer measurements (Nitsche and Brunn 2006) could also be used for unsteady flows, but are impractical for moving surfaces. In contrast, differential infrared thermography offers a contactless method of measuring the unsteady boundary layer transition without surface preparation for nonmetallic surfaces.

Infrared cameras have long been used for flow analysis, with the observations of Thomann and Frisk (1967) being the first published experiments. For a long time the only applications were in hypersonic research due to the low sensitivity of the cameras available (Gartenberg and Roberts 1992). The first subsonic investigations by Bouchardy et al. (1983) used a measurement of the recovery temperature in transonic flow to measure boundary layer transition. The work of Quast (1987) extended the application range by using a heated wall to measure heat transfer rather than recovery temperature, thus significantly increasing the signal available for measurement. Quast measured boundary layer transition and the laminar separation bubble at the boundary between laminar and turbulent boundary layer flow. The wall can be directly heated by thin films (Astarita and Cardone 2000), or indirectly using infrared lamps (Raffel and Merz 2014). An overview of some recent experiments separation and transition detection using these methods is given by Carlomagno and Cardone (2010). With the availability on the market of high-speed infrared cameras, they have been used for the detection of boundary layer transition in the rotating system where that would not previously have been possible due to the camera framing time, including on a helicopter hovering in ground effect (Richter and Schülein 2014).

Differential infrared thermography (DIT) is a new optical measurement technique based on infrared thermography suggested by Raffel and Merz (2014) for the unsteady boundary layer transition detection on pitching rotor blade airfoils. It has since been shown to work for boundary layer transition detection on rotating blades (Raffel et al. 2015) and a variant of the method has been shown to detect dynamic stall (Gardner et al. 2016). The technique is based

on the difference between two thermal measurement images and analyses differences in the surface temperatures existing between regions of laminar and turbulent flow in order to determine a moving boundary layer transition location.

This paper uses skin friction distributions from 2D steady and unsteady computations to produce computed DIT results. These can be used to show that DIT can be used to compute a mean boundary layer transition position (with a small systematic error), but not generally the start and end of the boundary layer transition region.

## 2 Experiment for DIT

The experiment for DIT which is computed in this paper was reported by Richter et al. (2016), and a summary is presented here. A 2D airfoil was installed in 1 m × 1 m adaptive-wall test section of the transonic wind tunnel Göttingen (TWG) with the 9% airfoil DSA-9A. The chord length was 300 mm and the airfoil spanned the whole width of the wind tunnel with small gaps of 1.5 mm between the airfoil ends and the wind tunnel wall. The airfoil was pitched using drive shafts at the  $c/4$  position which extended through the wind tunnel walls. For the test case presented here, the flow had  $M = 0.30$ ,  $Re = 1.8 \times 10^6$  and the pitching was sinusoidal at  $f = 6.6$  Hz with an amplitude of  $\alpha_1 = \pm 6^\circ$  around the mean angle of attack of  $\alpha_0 = 5^\circ$  for a movement of

$$\alpha = 5 + 6 \sin(2\pi 6.6t). \quad (1)$$

The airfoil was constructed using carbon-fibre-shells (Fig. 1) and was instrumented with Kulite pressure sensors directly under the shell surface and hot-film gauges. The hot-film gauges can be analysed to give boundary layer transition position, and the pressure sensors were also used to detect the boundary layer transition position using the  $\sigma C_p$  (standard deviation in pressure coefficient) method of Gardner and Richter (2015) for periodic flows.

The optical setup is shown in Fig. 2, where the surface of the airfoil is warmed by a 2-kW lamp and the infrared

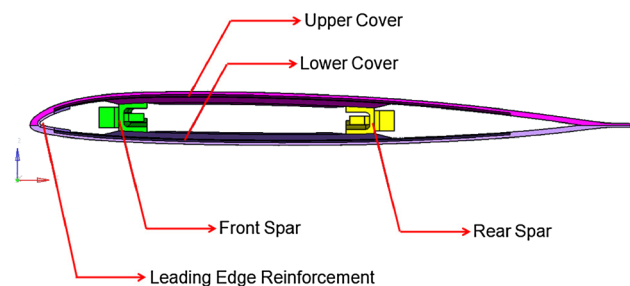


**Fig. 1** Cut through the airfoil showing the shell design. From Uenal and Grieb (2013)

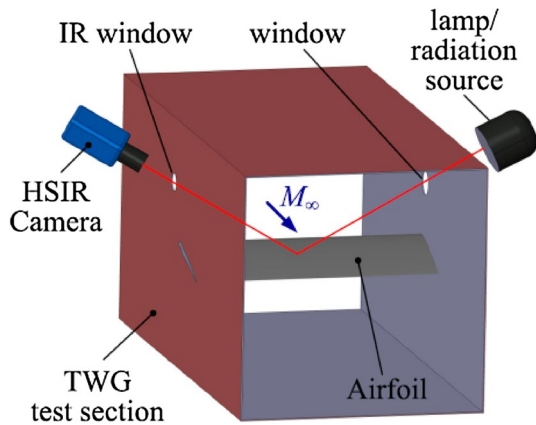


**Fig. 2** Sketch of the DIT experimental setup. From Richter et al. (2016)

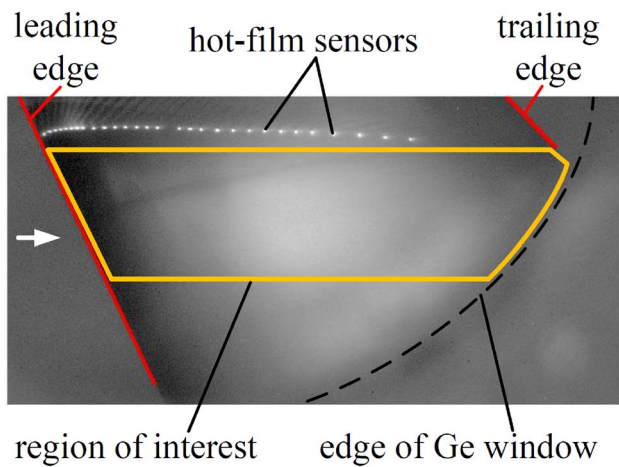


**Fig. 3** Example image acquired using the setup in Fig. 2. From Rafel et al. (2015)

emission of the surface is monitored by a high-speed infrared camera (FLIR SC7750-L) at 190 Hz. The high-speed infrared camera had a spectral range of 8.0–9.4  $\mu\text{m}$  detected by a cadmium–mercury–telluride FPA-detector. A focal length  $f_0 = 50$  mm lens with an aperture  $f_0/2.0$  was used. The data acquisition was performed with an integration time of 100  $\mu\text{s}$ , with a reduced detector region of  $640 \times 310$  px<sup>2</sup> and with an acquisition frequency of  $f_i = 190$  Hz. The DIT method evaluates intensity differences in the thermal images, it is not dependent on a calibration of the absolute temperature, but a temperatures are computed for comparison with the computation. The output of the camera was monitored with the data acquisition system for the pressure and angle of attack sensors so that a synchronization between the different systems could be achieved. The camera has a noise equivalent temperature difference (NETD) of <18 mK and images were acquired

using the “Altair” software. An example image is shown in Fig. 3.

The surface properties of the airfoil have a significant effect on the infrared signal measured, as recently explored by Simon et al. (2016). The airfoil surface was made of carbon-fibre reinforced plastic with a black colour, with an estimated emissivity of  $\epsilon = 0.95$  (Richter et al. 2016). An external layer of unenforced resin was painted into the mould during manufacture, and this layer was polished after the airfoil was removed from the mould. The airfoil is made of two 3 mm shells (top and bottom) constructed using the L285/H287 system of the firm Hexion. The mid-part of the airfoil is reinforced with a 1.5 mm spar (Fig. 1), for a total thickness of 5.5 mm. For the computations the thickness of 5.5 mm was used, however as will be seen later, the increased thickness of the surface shell due to the spar is not important for the computation of the surface temperatures. The fibre volume of the carbon-fibre shells is 45%. We do not have exact values for the thermal properties of the surface, but from the material data sheets of the epoxy and carbon fibre weaves estimate the thermal conductivity through the shell as  $k_v = 0.5$  W/m/K and along the shell as  $k_h = 7$  W/m/K, density  $\rho = 1180$  kg/m<sup>3</sup> and specific heat capacity  $C = 2300$  J/kg/K. Thus, the surface has low heat conductivity in the vertical direction.

### 3 Differential infrared thermography

Differential infrared thermography is a method of measuring the position of a moving boundary layer transition. The method is as follows:

- A series of high-speed infrared images of a surface are recorded.
- Difference-images are created by subtracting two images with a small image time separation  $t_2 - t_1 = 1/f_i$  from each other.
- Since the image time separation is small, most of each difference image has zero difference, but the area around the moving boundary layer transition has a nonzero difference.
- The area of nonzero difference is analysed to find the boundary layer transition position.

As discussed further in Richter et al. (2014), the definition of “boundary layer transition position” varies considerably in the literature. Particularly static hot-film experiments tend to set this point at 50% intermittency, but many CFD codes define the transition point to be where the turbulence production is no longer forced to zero. For this paper we will use the 50% intermittency point, which is in the middle of

the transition process, and equivalent to the point of maximum gradient in the skin friction coefficient  $C_f$ .

The basis of DIT is a heated model surface which establishes a temperature difference between the surface and the flow. This results in a heat transfer from the model into the flow, cooling the airfoil surface. Due to the difference in the heat exchange rate between laminar and turbulent flows, lower surface temperatures are produced by turbulent flow than by laminar flow.

The original paper DIT of Raffel and Merz (2014) assumed that the temperature distributions for a heated airfoil are purely a function of the local heat flux. Thus their concept sketch for the idea of DIT (Fig. 4) simply uses the distributions of  $C_f$  (or Stanton number) as temperature distributions. The assumptions (for boundary layer transition moving upstream) were:

- A DIT image is formed by subtracting Image 2 – Image 1, taken at times  $t_2$  and  $t_1$ .
- The lag of the temperature with respect to  $C_f$  is small.
- The end of the boundary layer transition region at  $t_1$  is the downstream end of the peak.
- The start of the boundary layer transition region at  $t_2$  is the upstream end of the peak.

This logic was followed by the same authors in a further paper (Raffel et al. 2015), where the start and end of boundary layer transition were found for a pitching airfoil and for a rotor with high cyclic pitch. In contrast to the theory, the experimental analyses detected the start and

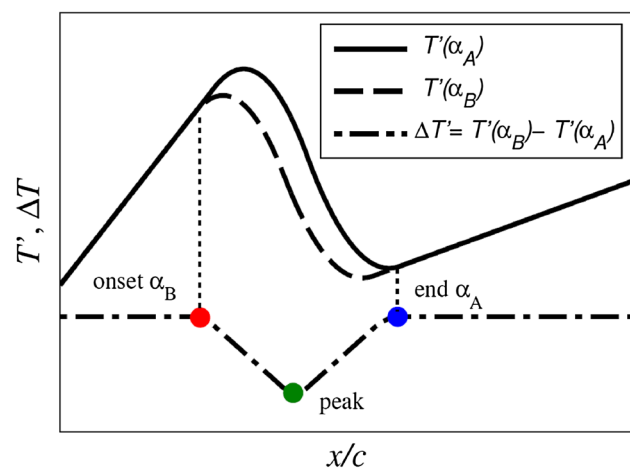


**Fig. 4** Original concept diagram of the operating principle of DIT. From Raffel et al. (2015)

end of boundary layer transition at 80% of the peak height (rather than 0% as expected). This change was necessitated to avoid experimental noise, but was not theoretically supported. Richter et al. (2016) showed by a comparison of hot-film,  $\sigma C_p$  and DIT measurements that measuring the position of the peak in  $\Delta T$  resulted in a boundary layer transition position at  $t = (t_2 + t_1)/2$  which was comparable to boundary layer transition measurements by the other methods. The results of Richter et al. (2016) were:

- The peak  $\Delta T$  is relatively easy to detect, except where the boundary layer transition reverses direction.
- The temperature lags  $C_f$  measurably.
- This leads to a different shape of the temperature peak than expected for  $\Delta C_f$ .
- The temperature lag is visible as a changing temperature while the boundary layer transition position is stationary. this leads to potential systematic errors around the region of boundary layer transition reversal.
- The temperature peak lags other methods of boundary layer transition detection, but the difference is within the experimental uncertainty ( $\Delta x/c = \pm 0.05$ ) and is certainly acceptable for a contactless measurement technique.

The earlier purely experimental work has noted a phenomenological correlation between the peak of  $\Delta T$  and boundary layer transition position, and this paper models the experiments numerically to explain the boundary layer transition phenomena noted.

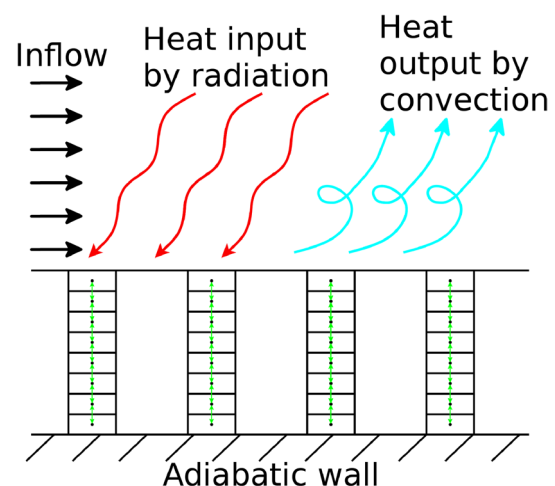


**Fig. 5** Sketch of the numerical scheme. Heat input at the surface is by radiation, and output is by convection to the flow at the surface. At the rear wall an adiabatic condition is held. The heat is only propagated in vertical stacks

#### 4 Surface temperature computation

A code was built to compute the surface temperature using the bulk properties of the surface and time-resolved  $C_f$  and  $C_p$  distributions as input. The surface temperature was computed using the assumption of 1D heat transfer, where heat is transported in the vertical direction only. The wall is discretised by cells in the depth, and the top cell has three inputs, as illustrated in Fig. 5:

- The heat flux via convection to the flow from the heated wall per unit area is described by:

$$\dot{q} = a_d(T_r - T), \quad (2)$$

where  $T$  is the wall temperature,  $T_r$  is the recovery temperature of the flow and  $a_d$  is the thermal diffusivity.

- The lamp heat flux  $H_L$  is a constant positive heat flux per unit area which is added to the surface at each time step.
- The heat flux between cells vertically is described by:

$$\frac{\partial T}{\partial t} = a_d \frac{\partial}{\partial z} \left( \frac{\partial T}{\partial z} \right). \quad (3)$$

The airfoil is then solved using a first-order finite-difference scheme. The following assumptions and simplifications are used:

- The airfoil is infinite in the  $y$ -direction (breadth).
- The recovery temperature  $T_r$  is computed using a constant recovery factor of 0.9, independent of whether the flow is laminar or turbulent.
- The thermal diffusivity,  $a_d$  is set using the Reynolds analogy to be:

$$a_d = 0.5 C_f \rho \nu C_{\text{air}}, \quad (4)$$

where  $C_f$  is the skin friction coefficient,  $\nu$  the flow velocity at the edge of the boundary layer and  $C_{\text{air}}$  is the heat capacity of air.

- The wall does not lose any energy by radiation.
- The wall thermal properties are homogeneous.

These assumptions are a considerable simplification of the physical situation. Nevertheless, all of these assumptions preserve the qualitative character of the surface temperature response. For example: treating a composite surface material as a homogeneous material will result in incorrect temperature distributions within the wall, but a qualitatively similar response of the surface temperature to flow changes.

As an output, the temperature distribution on the wall is computed as a function of time. The temperature differences are computed using a timestep equal to that from the experiment (data taken at  $f_i = 190$  Hz). The input time-resolved  $C_f$  and  $C_p$  distributions are computed using a URANS code.

#### 5 CFD computations of the skin friction and pressure coefficients

Computations were performed to produce wall skin friction coefficient  $C_f$  and wall pressure coefficient  $C_p$  data to produce synthetic data to use as an input for the computations. Since the skin friction data from the experiment was not available, a skin friction distribution as close as possible to that of the experiment was produced using a RANS solver. Although the attempt was made to closely reproduce the experimental condition, all of the conclusions of this paper are made solely using the CFD results, so any differences will be incidental.

The TAU unstructured flow solver (Schwamborn et al. 2008) was used on a 2D unstructured hybrid grid generated using the Centaur<sup>®</sup> grid generator. The surface of the airfoil was resolved with cells of maximum size 1% chord, reducing to 0.1% chord at the leading and trailing edges. The boundary layer was resolved using 60 layers, using the guidelines given by Richter et al. (2011) and Krumbein et al. (2009a), and the boundary layer transition position was computed using the 2D  $e^N$  transition code LILO (Schrauf 2006) coupled with the boundary layer code COCO (Schrauf 1998). The transition position is then fed back to the CFD code where wall nodes are set to be either “laminar” or “turbulent”. This results in a quantized boundary layer transition position which advances in steps, following the topology of the surface grid. This step behaviour meant that the analysis of the size of the image time separation ( $t_2 - t_1$ ) in Sect. 9 is not as smooth as could be hoped, especially for small time-offsets.

The computations were performed using the Spalart-Allmaras turbulence model (Spalart and Allmaras 1992) and the boundary layer transition was performed by switching on the turbulence production terms in the boundary layer at the “transition point”, as described in detail by Krumbein et al. (2009a, b). The unsteady computations used 1024 time steps per iteration with 800 inner iterations with a 4w multi-grid acceleration. The computation used a second-order time discretisation and a central second-order spatial scheme. The computations were run for three cycles, of which the last two cycles were periodic. The  $C_f$  and  $C_p$  data for the last cycle was written by the URANS solver (from surface pressure and vorticity data) at each time step and made available for the surface temperature code.

Figure 6 shows a comparison between the experimental and CFD movement and boundary layer transition positions, with the experimental position extracted using the  $\sigma C_p$  method (Gardner and Richter 2015), who estimate the error at  $\Delta x/c < 0.02$  in comparison with hot-film gauges. The CFD is tuned to reproduce the lift and transition position of the experiment knowing that wind tunnel corrections of up to  $\Delta \alpha = 1^\circ$  have been used in the TWG wind tunnel.

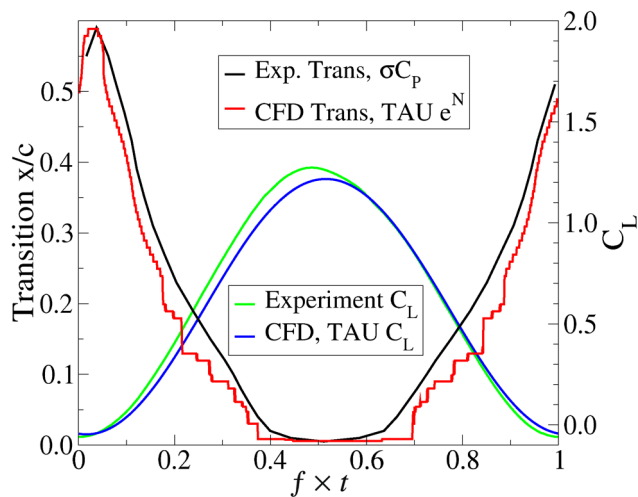


**Fig. 6** Comparison between the experiment and CFD

The CFD used a wind tunnel correction of the mean angle so that  $\alpha = 4.3^\circ \pm 6^\circ$  is computed rather than  $\alpha = 5^\circ \pm 6^\circ$  for the experiments. In both cases the Mach number was  $M = 0.3$  and the chord Reynolds number was  $1.8 \times 10^6$ . As detailed in AGARDograph 793 (Saric et al. 1994), the accepted selection method for  $N$ -factor is to use the method of Mack (1977), combined with a measurement of the turbulence level in the wind tunnel, with Eq. (5).

$$N = -8.43 - 2.4 \ln(\text{Tu}) \quad (5)$$

From turbulence measurements in the TWG wind tunnel, the freestream turbulence level at the  $M = 0.3$  conditions used by Richter et al. (2016) is  $\text{Tu} = 0.05\%$ , and thus the  $N$ -factor used was 10. The uncertainty of the boundary layer transition position in the CFD is estimated as  $\Delta x/c < 0.05$ . The comparison between the experiment and CFD is close enough that a qualitative similarity should be achieved, and the experiments can be used to calibrate the simulations. The boundary layer transition position in the CFD does not move smoothly, since each cell on the airfoil surface is constrained to be either laminar or turbulent, and this leads to steps in the transition position.

## 6 Coupled computations

The coupled computations were performed by first running the CFD code until a periodic solution was obtained. The 1024 values of  $C_p$  and  $C_f$  from the last cycle were then provided as a periodic input to the surface computation. The settings for the surface computations are shown in Table 1. The bulk coefficients for epoxy were used. The spatial and time-stepping discretisation of the wall was investigated. As shown in Fig. 7, the mean temperature of the wall took

**Table 1** Settings for surface computations

Cells in vertical direction	800
Cells in horizontal direction	140
Thickness of wall	5.5 mm
Time step for heat computation	$5 \times 10^{-5}$ s
Time step from CFD	$1.5 \times 10^{-4}$ s
Total time of computation	1000 s
Wall material	Epoxy
$k_v$	0.5 W/m/K
$C$	2300 J/kg/K
$\rho$	1180 kg/m <sup>3</sup>
Lamp heat flux $H_L$	2000 W/m <sup>2</sup>
Freestream static temperature	294 K
Freestream total temperature	300 K

1000 s to converge, thus all computations in this paper were run for a time of 1000 s. The convergence of the wall temperature was not monitored during the experiments, but about 5 min of warm-up time was allowed before the first measurement. The computations on the wall are discretised in time using a time-step of  $5 \times 10^{-5}$  s, and the time-step of the aerodynamic data was  $1.5 \times 10^{-4}$  s, thus three heat-propagation time steps are taken for each aerodynamic time-step. The aerodynamic data is interpolated in time for the intermediate time-steps. The time-stepping convergence was investigated, as shown in Fig. 8, showing that all time step sizes smaller than the aerodynamic time step were equivalent. Eder (2016) suggests that for static computations where the flow does not change, that a time step of  $3 \times 10^{-2}$  s is sufficient. Thus the only requirement for the time step size is that the aerodynamic solution (time step  $1.5 \times 10^{-4}$  s) is transmitted to the surface cells. The grid-convergence in the vertical direction was investigated, as shown in Fig. 9. Since the  $\Delta T$  peak size and position is effectively identical between grid sizes of 400 and 800 per vertical stack, the grid size of 800 cells per vertical stack (cells of 6.8  $\mu\text{m}$ ) is sufficient to discretise the heat flux.

Figure 10 shows  $C_f$ ,  $C_p$  and temperature distributions on the suction side of the airfoil for the same instant. After the suction peak,  $C_p$  (plotted in reversed axes) increases toward the airfoil trailing edge. The skin friction coefficient,  $C_f$ , also falls, but has a rise around  $x/c = 0.15$ , associated with the boundary layer transition. The surface temperature increases toward the trailing edge, and the temperature in the middle of the airfoil of 307 K is consistent with the 306 K estimated from the infrared measurements. The rapid rise in temperature near the rear edge of the airfoil is due to the low heat transfer away from the airfoil by the thickened boundary layer near the trailing edge of the airfoil which is starting to approach stall. At the airfoil leading edge the surface temperature is approximately the same as the freestream

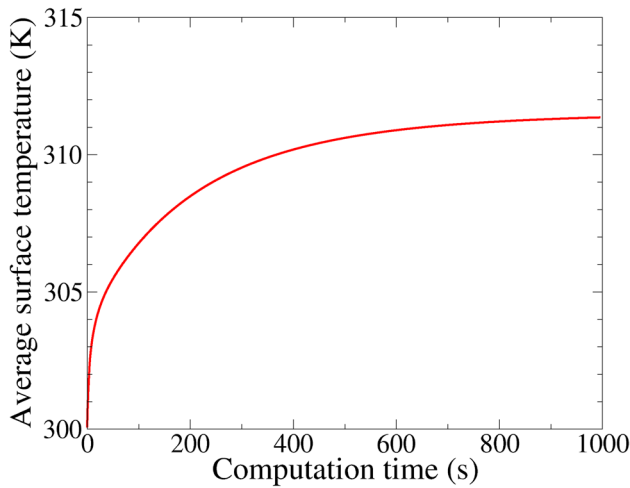


**Fig. 7** Time convergence of the average wall temperature

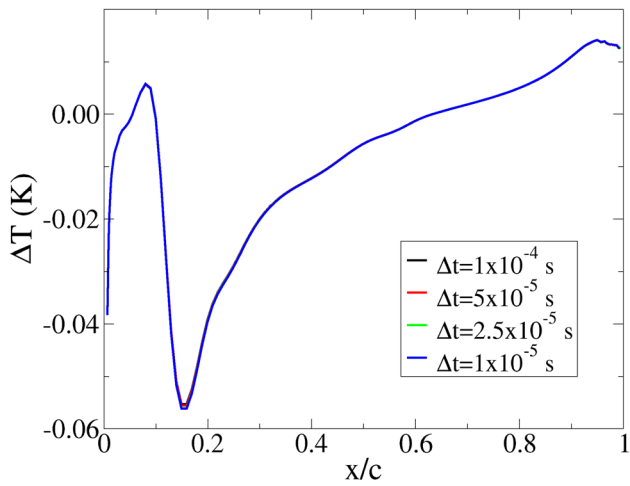


**Fig. 8** Time step convergence effect on  $\Delta T$ . A time step of  $5 \times 10^{-5}$  s was used for computations shown in this article

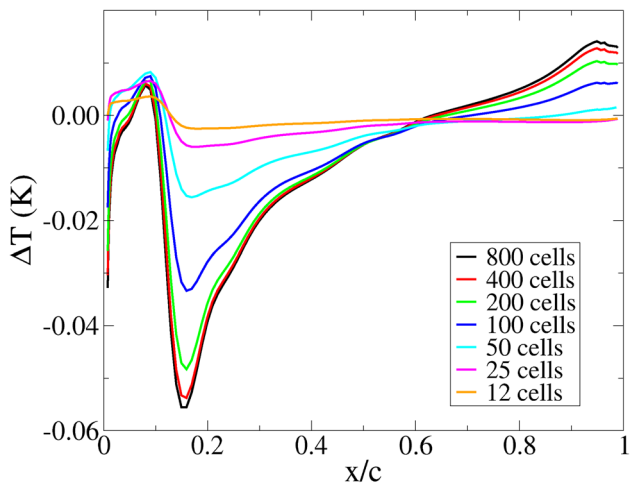


**Fig. 9** Grid convergence effect on  $\Delta T$ . 800 cells was used for computations shown in this article

stagnation temperature of 300 K. Since Fig. 10 is for an unsteady flow, the temperature step due to boundary layer transition is very small and the step typical of transition on a static airfoil is not present. Thus DIT is used as the transition position can only be extracted from the temperatures by using differences.

As shown in Fig. 11, the experimental and numerical data for the temperature difference,  $\Delta T$ , agree well in amplitude, but the downstream part of the temperature difference has a different shape in the experiments than in the computations. The reasons for the poor agreement outside the peak region are presently unknown, but are considered to be a combination of unmodelled effects (emissivity variation with angle of incidence, internal flow in the airfoil) and unevenness of the lamp illumination of the airfoil. The peak positions

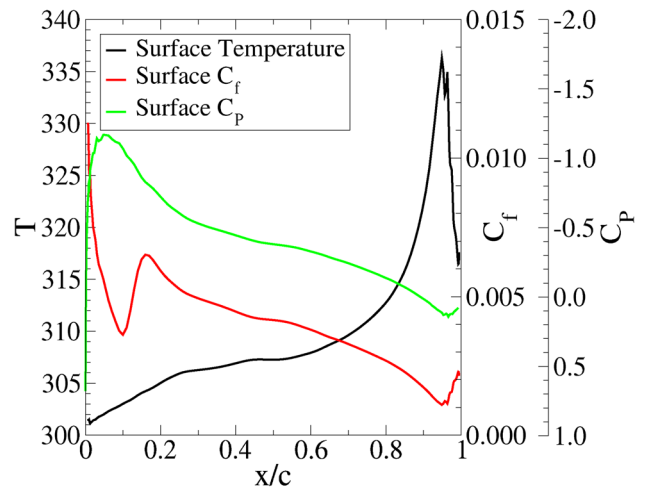


**Fig. 10** Example distributions of temperature,  $C_f$  and  $C_p$

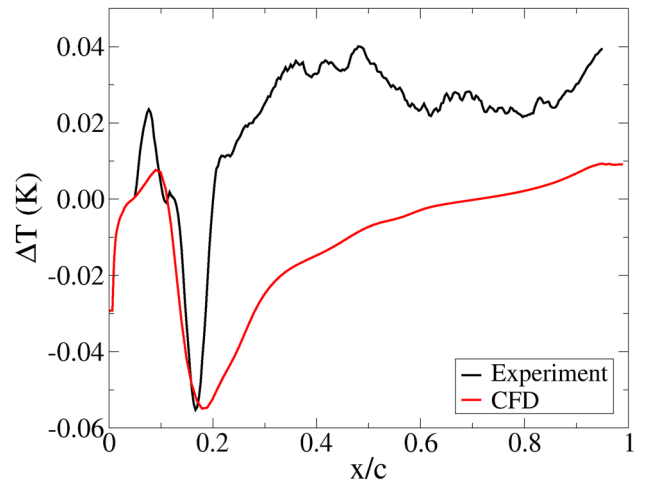


**Fig. 11** Comparison between Experiment and CFD temperature distributions at  $\alpha = 3.25^\circ$  on the upstroke

agree well, and the agreement is sufficient to validate the numerical approach.

### 7 Effect of the finite temperature delay

Boundary layer transition causes a sudden increase in the skin friction, which is associated with a change in surface heat transfer. The distribution of  $C_f$  for boundary layer transition with the airfoil pitching up and transition on the suction side moving towards the leading edge with advancing time is shown at three different times in Fig. 12, along with the difference in  $C_f$ . It can be noted that these computed values agree well with the concept sketch of Raffel et al. (2015) shown in Fig. 4. Raffel et al. posited that the start and end of boundary layer transition are visible as the start and end of the  $C_f$  peak, and this is true, although the exact definition of the peak ends is difficult. Note particularly that a visible difference between the two  $C_f$  distributions continued downstream of the end of transition for  $t_1$ . Perhaps more practically, Richter et al posited that the peak in  $\Delta C_f$  corresponds to the boundary layer transition position at  $t = (t_2 + t_1)/2$ . Although there is no particular reason why this must be the case, it appears to be true for the cases investigated in this paper.

The definition of a boundary layer transition point as applied to CFD can be at variance to the experimentally applied maximum intermittency or maximum gradient in  $C_f$ . Figure 13 shows a comparison between different computations of the transition points from computational data. The lines are defined by:

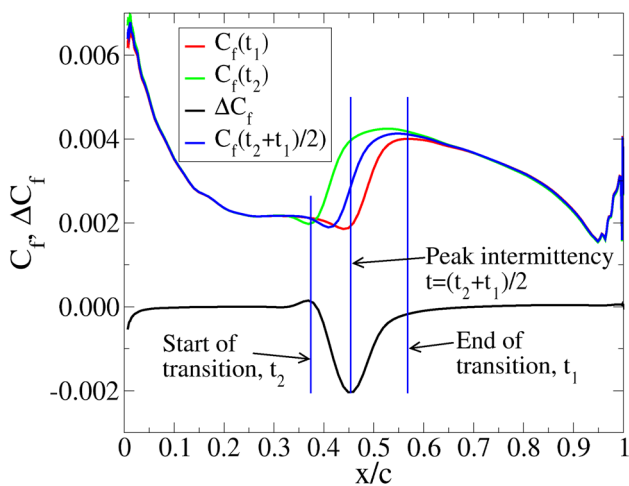


**Fig. 12** For the dynamically pitching airfoil the difference image  $\Delta C_f$  is produced using a difference between the  $C_f$  distributions at times  $t_1$  and  $t_2$ , with the airfoil pitching up and boundary layer transition on the suction side moving towards the leading edge with advancing time

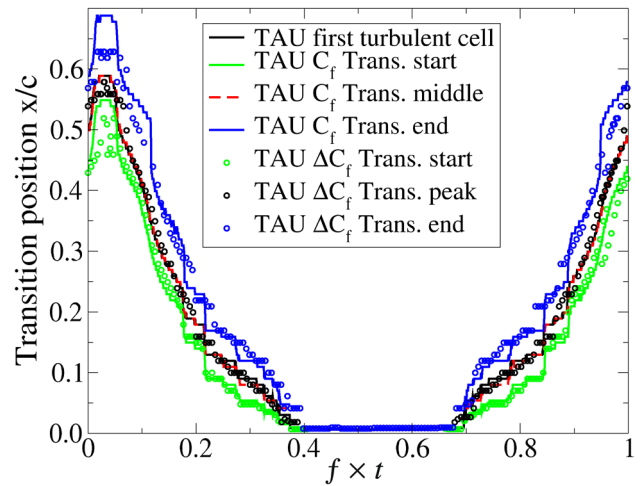


**Fig. 13** Comparison of boundary layer transition points from the computations

- The official boundary layer transition point from the computation is the point at which the turbulence production is switched on, as noted by the black line.
- The upstream (green line) and downstream (blue line) ends of the boundary layer transition region are determined as the points of zero gradient in the  $C_f$  curve. The start of boundary layer transition can be noted as the point where the gradient of  $C_f$  passes zero on the upstream side of the transition point, and the downstream end is where the gradient in  $C_f$  passes zero on the downstream side.
- The boundary layer transition point middle (red dashed line) is computed as the point of maximum gradient in the  $C_f$  curves (intermittency is not available in the computations). The turbulence production has an upstream effect which shifts the start of transition upstream of the point where the turbulence production is switched on in the computation and results in the maximum gradient in  $C_f$  correspond well to the point where turbulence production is switched on.
- For the  $\Delta C_f$  curves, the start (green dots) and end (blue dots) of the  $\Delta C_f$  peak are detected as peaks in the second derivative of the  $\Delta C_f$  curve. Using the second derivative in  $\Delta C_f$  to detect the start and end of the peak is not physically based, but serves as a replacement for the sharp start and end of the curve, as postulated in Fig. 4. The agreement with the start and end as computed from the  $C_f$  curve is relatively good, even considering problem areas as near  $f \times t = 0.7$  where the automated detection cannot detect the second derivative correctly.
- The peak in  $\Delta C_f$  (black dots) fits well to the boundary layer transition position from the solver and that from the  $C_f$  maximum gradient well, and corresponds to the middle of transition or maximum intermittency.



The analysis of  $C_f$  above shows that the basic idea of Raffel and Merz (2014) is correct; however, the  $C_f$  distribution is not directly measured using IR thermography, rather the temperature distribution is measured. Figure 14 shows a comparison between temperature  $\Delta T$  and skin friction  $\Delta C_f$  differences at an acquisition rate of  $f_i = 190$  Hz on the upstroke. Figure 15 shows the same figure for the downstroke. The  $\Delta T$  are negative when the  $\Delta C_f$  peaks are positive (and the opposite), since increased  $C_f$  increased the cooling of the airfoil and reduces the temperature. The  $\Delta T$  peak positions always lag the  $\Delta C_f$  peak positions in time, and the shape of the  $\Delta T$  peaks is different than the  $\Delta C_f$  peaks, with the  $\Delta T$  peaks having a sharp edge in the direction of travel and a long tail in the opposite direction. Thus in the downstroke, the downstream edges of the peak are sharp and the upstream edges are blurred, and the upstream edge is sharp on the upstroke. With changing angle of attack, the position of the stagnation point on the airfoil changes significantly, and this results in a change in the wetted length of the airfoil (by about  $x/c = 0.1$ ). Additionally, the Mach number and local density of the flow over the airfoil change depending on the angle of attack. The result is that all positions on the airfoil have a sinusoidal temperature change during a pitching cycle, and this is visible in the  $\Delta T$  positions outside the peak positions. The width of the  $\Delta T$  peak increases with increasing length of the boundary layer transition region, but the start and end of the transition region cannot be extracted as a feature from the  $\Delta T$  distribution.

The peak of the  $\Delta T$  distribution was extracted and plotted in Fig. 16. The cyan crosses are the most reliable method of boundary layer transition position detection and are extracted by selecting the minimum of  $\Delta T$  on the upstroke and the maximum of  $\Delta T$  on the downstroke, switching when the physical direction of airfoil pitching

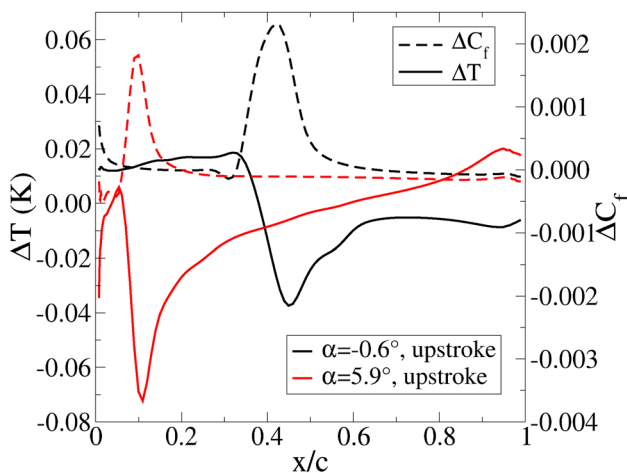


Fig. 14 Comparison of  $\Delta T$  and  $\Delta C_f$  distributions during the upstroke

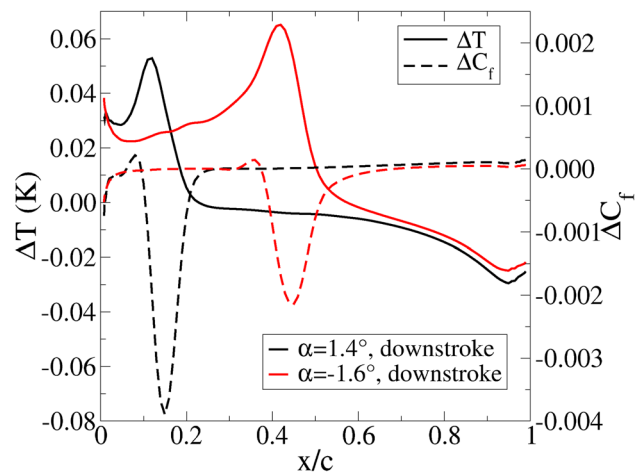


Fig. 15 Comparison of  $\Delta T$  and  $\Delta C_f$  distributions during the downstroke

changed. A systematic error is introduced due to the time lag of  $\Delta T$  behind  $\Delta C_f$ , but this is constrained to 1.5 ms, or an error in the transition position of  $x/c = 0.05$ . The 1.5 ms delay is uniform over the whole pitching cycle, independent of pitching rate  $\dot{\alpha}$  or boundary layer transition position. An alternative method of boundary layer transition position detection was used by Richter et al. (2016) and compares the absolute sizes of the positive and negative  $\Delta T$  peaks when the median of the whole  $\Delta T$  distribution is subtracted. This method is more generalizable, since it does not rely on a priori knowledge of the direction of boundary layer transition movement, and at most points the same result is achieved as simply using the maxima of  $\Delta T$ . At the red circles in Fig. 16, a different transition position is systematically predicted. This is related

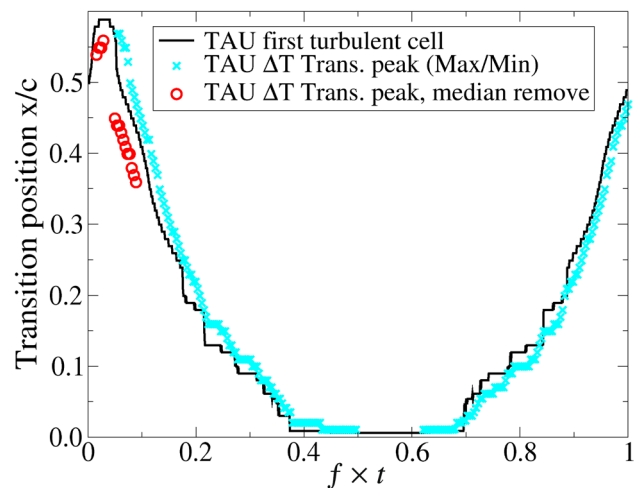
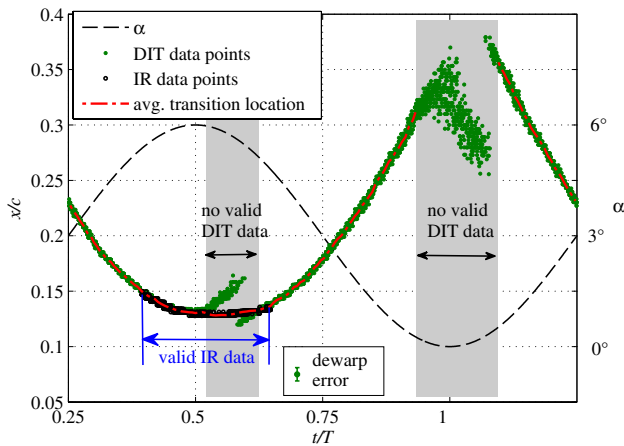


Fig. 16 For the same case as Fig. 13, the boundary layer transition position as given by the peak of temperature

to the problem of detection of the boundary layer transition position when the transition position is momentarily unmoving. Figure 17 shows the analysis from Richter et al. (2016), showing the experimentally detected points for boundary layer transition using DIT. At the upstream-most point of boundary layer transition no transition point could be found, but the static IR images could be analysed to give a boundary layer transition position. At the downstream-most point of boundary layer transition the detected transition has a systematic error, and the static IR data was not usable due to the low local wall shear stress.

Figure 18 shows  $\Delta T$  distributions around the downstream point where the boundary layer transition direction changes, from downstream movement to upstream movement. It can be seen that at the moment of reversal ( $f \times t = 0$ ), where the boundary layer transition position movement is zero, a strong positive peak in  $\Delta T$  is visible. This is different to the prediction of Raffel and Merz (2014), who would have expected zero signal at this position. After this time, the positive peak in  $\Delta T$  rapidly reduces, and the new negative peak in  $\Delta T$  caused by the upstream movement of the boundary layer transition position is superimposed on the old  $\Delta T$  distribution. By  $f \times t = 0.036$ , the negative temperature peak is visible, and the transition is moving upstream with the  $\Delta T$  peak position slightly lagging the true transition position. In the change between the positive and negative  $\Delta T$  peaks, there is a region where both a positive and a negative peak are visible. The positive peak is not associated with the boundary layer transition position, and a detection algorithm which follows this peak leads to a detection of the transition



**Fig. 17** Figure from Richter et al. (2016), showing the experimentally detected points for boundary layer transition using DIT. The systematic error is due to the use of  $\max(\text{abs}(\Delta T_{\min} - \Delta T_{\text{median}}), \text{abs}(\Delta T_{\max} - \Delta T_{\text{median}}))$  as the detection criterion for the transition point. The alternative is to always use  $\Delta T_{\min}$  on the upstroke and  $\Delta T_{\max}$  on the downstroke, switching as the movement of the airfoil switches. The difference between these two approaches can be seen in Fig. 16

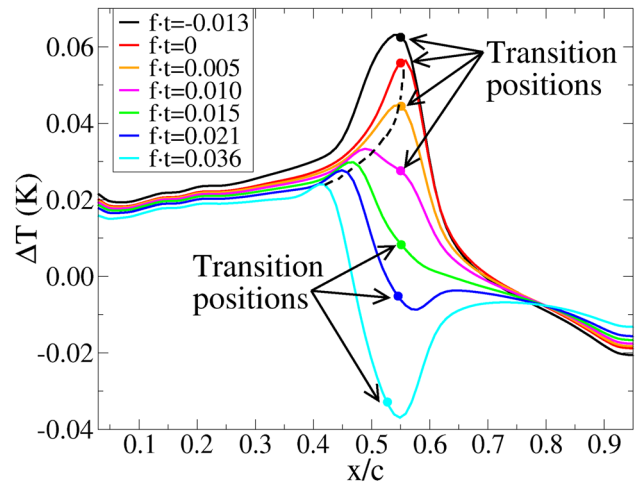


**Fig. 18** Illustration of the problem with peak detection at the point of reversal in the direction of travel of the boundary layer transition position. Due to the delay of the temperature distribution behind the  $C_f$  distribution, an incorrect peak is produced, which moves upstream on the airfoil

position rapidly moving upstream (see the black dotted line), whereas in reality it is nearly stationary. Adding knowledge about the direction of boundary layer transition travel means that up to  $f \times t = 0$   $\Delta T_{\max}$  is detected, and thereafter  $\Delta T_{\min}$ . This means that the false peak is not detected, but that at times less than  $f \times t = 0.021$  no valid negative peak can be found, and thus boundary layer transition cannot be detected using DIT.

### 8 Effect of material selection

The selection of an appropriate surface material obviously has an effect on the surface temperature distribution response to dynamically changing flows. Simon et al. (2016), noted that the peak-to-peak height of the temperature response to a pulse input was higher by a factor of roughly two for thin surface films (with low thermal mass) heated resistively or radiatively compared to when solid aluminium and a foil heater (with higher thermal mass) were used. Generally, lower heat capacity materials and better thermal insulators should give a larger signal. To investigate this effect, the surface temperature was computed for the range of material constants in Table 2. Particularly materials 3–7 represent machinable materials which could reasonably be used for a wind tunnel model, either as full material, or as a surface covering with a foil or contact sheet. Table 2 lists approximate bulk material constants, and it is questionable whether for materials 1 and 2, expanded polystyrene or cork have these properties on a small scale.

The material selection can effect both the size of the  $\Delta T$  peak signal and the time delay between the peak position and

**Table 2** Example materials

Ref. #	$k_v$ (W/m/K)	$C$ (J/kg/K)	$\rho$ (kg/m <sup>3</sup> )	Example material
1	0.05	1300	20	Expanded polystyrene
2	0.05	1900	250	Cork
3	0.1	1300	1100	Polystyrene
4	0.15	1400	1100	Mylar®
5	0.2	1500	1200	Plexiglass®
6	0.3	2300	1200	Polyethylene
7	0.5	2300	1180	Epoxy
8	0.6	2800	2200	Pyrex® glass

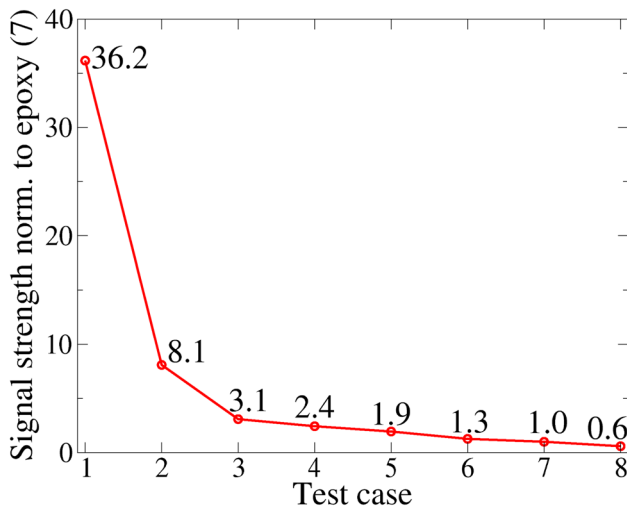


**Fig. 19** Comparison of the signal strength in the temperature difference images for the materials in Table 2

the position of boundary layer transition. The peak height is compared for the different materials in Fig. 19. With the exception of materials 1 and 2, the variation in signal strength is limited to a factor of three compared to epoxy, of the same order of magnitude as the factor of two seen by Simon et al. (2016). Interesting to note is that epoxy is one of the worst materials in terms of signal strength. In contrast to these results, the effect of different materials on the time delay between the  $\Delta T$  peak and the true boundary layer transition position is negligible. Figure 20 shows that for materials 3–8 the time delay between the  $\Delta T$  peak and the true boundary layer transition position is 1.4–1.5 ms, and for material 2 it is 1.3 ms. Although generally better thermal insulators had a faster response, the effect is not significant except for material 1. The importance of the small-scale material properties (as opposed to bulk properties) is made clear in Fig. 21. Here the variation in temperature over the thickness of the surface is plotted for epoxy, for a cell at  $x/c = 0.56$ . It can be seen that the variation is restricted to the first 0.5 mm, with the majority of the variation in the

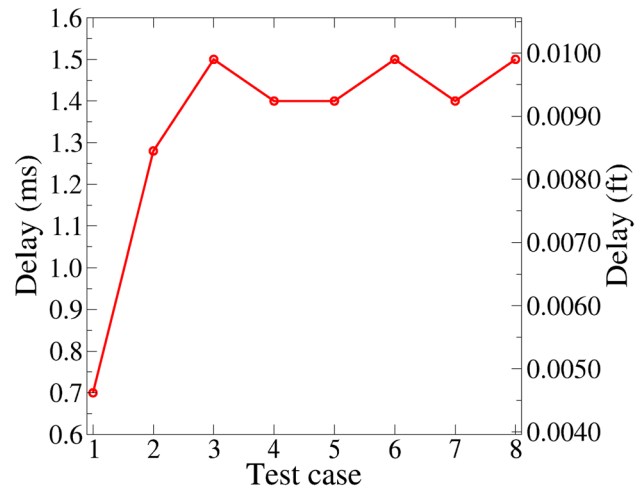


**Fig. 20** Comparison of the time delay in the detected boundary layer transition position compared to the true transition position for the materials in Table 2

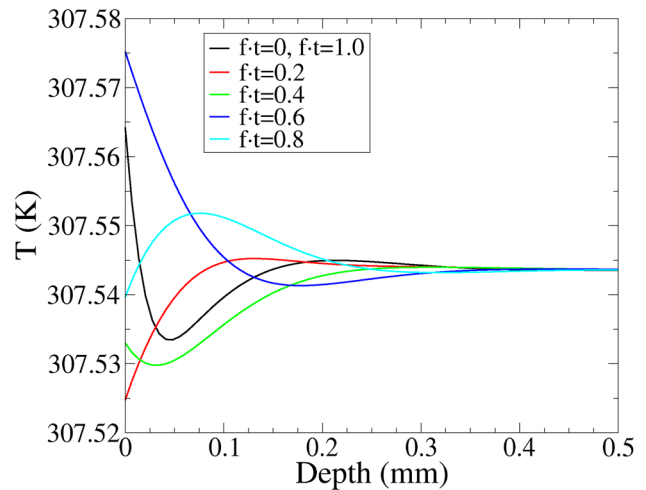


**Fig. 21** Variation of temperature in a single stack of cells near the airfoil leading edge over a pitching cycle for material 7 (epoxy)

first 0.1 mm. Generally the heat conduction is a small-scale phenomenon, and any large-scale heat conduction occurs on much longer time-scales than those of the unsteady flow, as also indicated by the heating time curve in Fig. 7. This investigation indicates that the use of paint or contact sheets with a thickness of 100–200  $\mu\text{m}$  is probably sufficient to control the surface properties.

### 9 Effect of image time separation

The image time separation  $t_2 - t_1 = 1/f_i$  can be varied in the experiments by increasing the camera framing rate or (for periodic processes) by selecting images which are closer

together in the period. Figure 22 shows a comparison of the  $\Delta T$  distribution on the airfoil due to different image time separations, for a test case where the transition position is advancing toward the leading edge and the detected transition position is downstream of the true transition position. With increasing separation the strength of the observed peak increases, since the surface has had more time to react to the changing flow. However a non-intuitive effect is observed, in that larger image time separations result in a greater delay between the position of the  $\Delta T$  peak and the true transition position. Two effects together cause this result: Smaller temperature differences occur more quickly after a flow change, and thus a smaller temperature difference is inherently less lagged. Second, the difference between the two images is a result of the complete flow history between the two time points. This results in a difference in the complete shape of the  $\Delta T$  distribution (note the rise and movement in the positive peak near  $x/c = 0.2$  and the negative peak near  $x/c = 0.9$ ), which results in a distortion of the primary  $\Delta T$  peak shape.

The peak shape distortion results in a significant change in the time delay in the detected boundary layer transition position compared to the true transition position, as shown in Fig. 23. It must be emphasised here that the quantization of the transition position (see Fig. 6) resulted in the results for different image time separations not being as comparable as could be hoped, especially for small image time separations. Figure 23 shows that the relative delay decreases with decreasing image time separation (Black line). The signal strength also decreases with decreasing image time separation (red line), and due to the inclusion of the complete flow history between the two time points, the signal strength should be expected to increase less than linearly for large image time separations. It would be expected that both lines

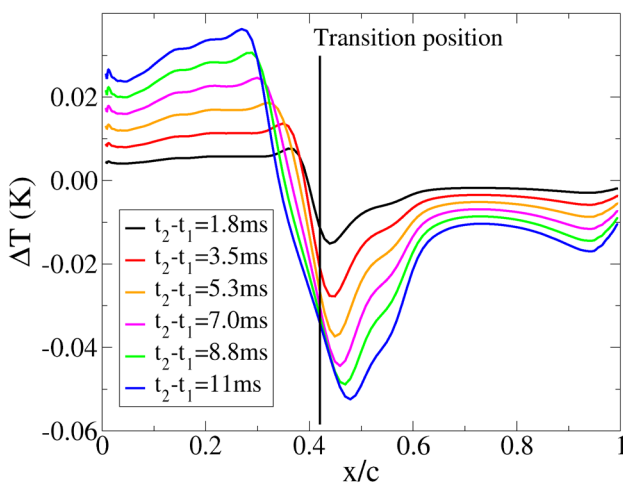


Fig. 22 Effect of the image time separation on the  $\Delta T$  distribution

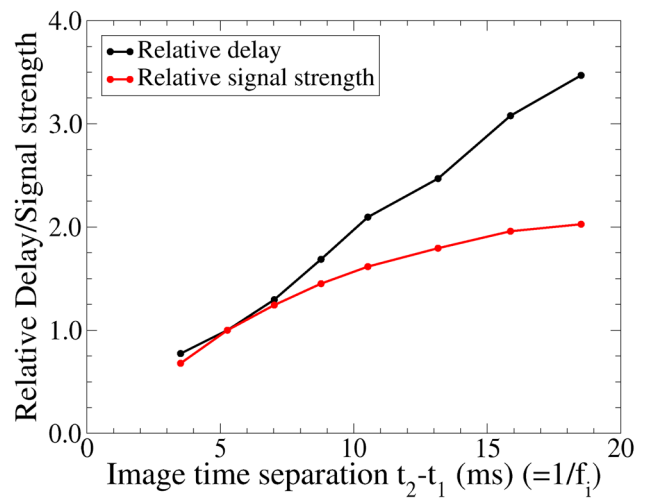


Fig. 23 Effect of the image time separation on the signal strength and measurement delay for the computations

on this figure should pass through (0, 0). The experimental point for  $\alpha = 5^\circ \pm 6^\circ$  had an insufficient signal-to-noise ratio to allow this kind of analysis so an analysis for  $\alpha = 3^\circ \pm 3^\circ$  is shown in Fig. 24. The experimental data shows the same qualitative changes as the computations when the image time separation is changed.

This shows that the correct measurement method for DIT is to reduce the image time separation until the signal-to-noise is at a minimum acceptable level. Improvements in the signal by using surface coatings, increased heating (within limits which do not affect the boundary layer transition position) or a reduction in noise by the use of multiple images or the averaging of multiple pixels in a single image should be used to reduce the image time separation.

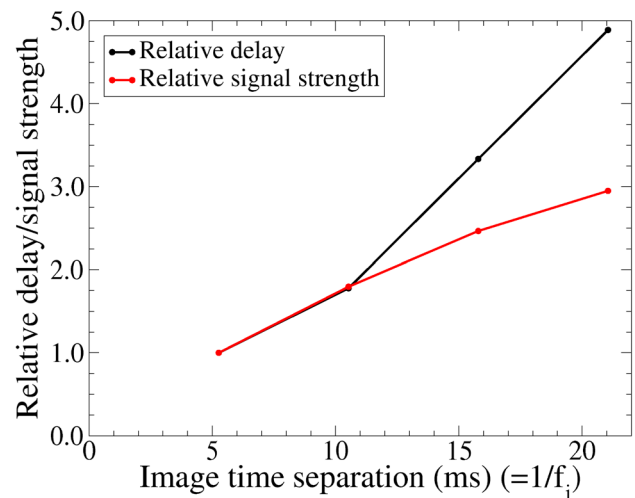


Fig. 24 Effect of the image time separation on the signal strength and measurement delay for an experimental point with  $\alpha = 3^\circ \pm 3^\circ$  at  $f = 6.6$  Hz

This method will improve the quality of the boundary layer transition position measurement but not the image quality.

## 10 Conclusions

An analysis of Differential Infrared Thermography (DIT) for the detection of dynamically moving boundary layer transition positions has been performed for a pitching airfoil with Mach 0.3, Reynolds number  $1.8 \times 10^6$  with sinusoidal pitching at  $\alpha = 5^\circ \pm 6^\circ$ . The surface temperature was computed using a finite difference method, and flow input from CFD. The temperature differences,  $\Delta T$ , were generated to match the experimental camera frame rate of  $f_i = 190$  Hz. The important results were:

- The assertion of Richter et al. (2016) that the  $\Delta T$  peak indicates the boundary layer transition position is confirmed.
- The  $\Delta T$  peak lags the true boundary layer transition position, and this lag is insensitive to the selection of the surface material but can be reduced by reducing the image time separation.
- The dynamic temperature variation detected by DIT only affects the top 0.5 mm of the surface, with the main variation much closer to the surface. Thus the use of paint or contact sheets with a thickness of 100–200  $\mu\text{m}$  is probably sufficient to control the surface properties. The  $\Delta T$  peak signal can be improved by a factor of three by the selection of surface materials with reduced heat capacity and heat transfer.
- Decreasing the image time separation results in a reduction of the  $\Delta T$  peak lag with respect to the true boundary layer transition position and an increase in the  $\Delta T$  signal strength. Improvements in the signal by using surface coatings or reduction of the noise should be used to reduce the image time separation used, since this will result in a more accurate measurement of the boundary layer transition position.
- When the boundary layer transition position is moving, the detection of the  $\Delta T$  peak is insensitive to the method used. When the direction of movement of the boundary layer transition direction reverses, the detection of the  $\Delta T$  peak position is difficult, and some algorithms result in a systematic error in the boundary layer transition position.
- Contrary to the original assertions of Raffel and Merz (2014), the start and end of the peak in  $\Delta T$  are not correlated with a particular position in the boundary layer transition process. Despite this, a wider peak indicates a longer boundary layer transition length.

The usefulness of DIT for the detection of dynamic boundary layer transition position is confirmed, and the

accuracy is acceptable for a non-contact optical method which is capable of detecting 3D boundary layer transition positions.

**Acknowledgements** This work was done within the DLR projects FAST-Rescue and STELAR.

## References

- Astarita T, Cardone G (2000) Thermofluidynamic analysis of the flow in a sharp 180 degrees turn channel. *Exp Therm Fluid Sci* 20(3–4):188–200
- Bouchardy A-M, Durand G, Gauffre G (1983) Processing of infrared thermal images for aerodynamic research. *Appl Digit Image Process* 397:304–309
- Carlomagno GM, Cardone G (2010) Infrared thermography for convective heat transfer measurements. *Exp Fluids* 49(6):1187–1218
- Døssing M (2008) High frequency microphone measurements for transition detection on airfoils. *Risø-R-1645(EN)*
- Du Z, Selig MS (2000) The effect of rotation on the boundary layer of a wind turbine blade. *Renew Energy* 20(2):167–181
- Eder C (2016) Analyse der Differenzinfrarotthermographie (Engl: Analysis of differential infrared thermography). Masters thesis, University of the Bundeswehr, Munich, August 2016
- Gardner AD, Richter K (2015) Boundary layer transition determination for periodic and static flows using phase-averaged pressure data. *Exp Fluids*. doi:10.1007/s00348-015-1992-9
- Gardner AD, Wolf CC, Raffel M (2016) A new method of dynamic and static stall detection using infrared thermography. *Exp Fluids* 57(9):2016. doi:10.1007/s00348-016-2235-4
- Gartenberg E, Roberts AS Jr (1992) Twenty-five years of aerodynamic research with infrared imaging. *J Aircr* 29(2):161–171
- Heister CC (2013) Numerical investigation of laminar-turbulent transition mechanisms for helicopter rotors in forward flight. In: American helicopter society 69th annual forum, Phoenix, Arizona, May 21–23, 2013
- Krumbein A, Krimmelbein N, Schrauf G (2009a) Automatic transition prediction in hybrid flow solver, part 1: methodology and sensitivities. *J Aircr*. doi:10.2514/1.39736
- Krumbein A, Krimmelbein N, Schrauf G (2009) Automatic transition prediction in hybrid flow solver, part 2: practical application. *J Aircr*. doi:10.2514/1.39738
- Langtry R, Gola J, Menter F (2006) Predicting 2D airfoil and 3D wind turbine rotor performance using a transition model for general CFD codes. In: 44th AIAA aerospace sciences meeting and exhibit, p 395
- Lanzafame R, Mauro S, Messina M (2013) Wind turbine CFD modeling using a correlation-based transitional model. *Renew Energy* 52:31–39
- Mack LM (1977) Transition prediction and linear stability theory. In: AGARD Conf. Proc. no 224, Paris, 1977 (also **JPL Publication 77-15, 1977**)
- Nitsche W, Brunn A (2006) Strömungsmesstechnik (Engl. Flow measurement techniques). Springer, Berlin. ISBN: 978-3540209904
- Quast A (1987) Detection of transition by infrared image technique. In: 12th international congress on instrumentation in aerospace simulation facilities (ICIASF 87), Williamsburg, VA, 22–25 June 1987, pp 125–134
- Richards EJ, Burstall FH (1945) The “China Clay” method of indicating transition. *ARC R&M*, No. 2126, HM Stationery. Office 19:1945
- Richter K, Le Pape A, Knopp T, Costes M, Gleize V, Gardner AD (2011) Improved two-dimensional dynamic stall prediction with

- structured and hybrid numerical methods. *J Am Helicopter Soc.* doi:[10.4050/JAHS.56.042007](https://doi.org/10.4050/JAHS.56.042007)
- Richter K, Koch S, Gardner AD, Mai H, Klein A, Rohardt C-H (2014) Experimental investigation of unsteady transition on a pitching rotor blade airfoil. *J Am Helicopter Soc* 59(1):2014. doi:[10.4050/JAHS.59.012001](https://doi.org/10.4050/JAHS.59.012001)
- Richter K, Schülein S (2014) Boundary-layer transition measurements on hovering helicopter rotors by infrared thermography. *Exp Fluids.* doi:[10.1007/s00348-014-1755-z](https://doi.org/10.1007/s00348-014-1755-z)
- Richter K, Wolf CC, Gardner AD, Merz CB (2016) Detection of unsteady boundary layer transition using three experimental methods. In: 54th AIAA aerospace sciences meeting, San Diego (CA), USA, 4–8 January 2016, AIAA-2016-1072
- Raffel M, de Gregorio F, de Groot K, Schneider O, Gibertini G, Seraudie A (2011) On the generation of a helicopter aerodynamic database. *Aeronaut J* 115(1164):103–112. doi:[10.2514/1.J053235](https://doi.org/10.2514/1.J053235)
- Raffel M, Merz CB (2014) Differential infrared thermography for unsteady boundary-layer transition measurements. *AIAA J* 52(9):2090–2093. doi:[10.2514/1.J053235](https://doi.org/10.2514/1.J053235)
- Raffel M, Merz CB, Schwermer T, Richter K (2015) Differential infrared thermography for boundary layer transition detection on pitching rotor blade models. *Exp Fluids.* doi:[10.1007/s00348-015-1905-y](https://doi.org/10.1007/s00348-015-1905-y)
- Saric et al (1994) Progress in transition modelling. AGARD-R-793
- Schrauf G (1998) COCO: a program to compute velocity and temperature profiles for local and nonlocal stability analysis of compressible, conical boundary layers with suction. Center of Applied Space Technology and Microgravity Technical Rept., Nov 1998
- Schrauf G (2006) LILO 2.1 user's guide and tutorial. Geza Schrauf Stability Computations Tech. Rept. 6 (**originally issued Sept. 2004, modified for Ver. 2.1 July 2006**)
- Schülein E (2014) Optical method for skin-friction measurements on fast-rotating blades. *Exp Fluids.* doi:[10.1007/s00348-014-1672-1](https://doi.org/10.1007/s00348-014-1672-1)
- Schultz DL, Jones TV (1973) Heat-transfer measurements in short-duration hypersonic facilities. AGARDograph 165
- Schwamborn D, Gardner AD, von Geyr H, Krumbein A, Lüdeke H, Stürmer A (2008) Development of the TAU-code for aerospace applications. In: 50th NAL INCAST (international conference on aerospace science and technology), Bangalore, India, June 26–28, 2008
- Simon B, Filius A, Tropea C, Grundmann S (2016) IR thermography for dynamic detection of laminar-turbulent transition. *Exp Fluids.* doi:[10.1007/s00348-016-2178-9](https://doi.org/10.1007/s00348-016-2178-9)
- Spalart PR, Allmaras SR, (1992) A one-equation turbulence model for aerodynamic flows, AIAA 1992-0439. In: AIAA 30th aerospace sciences meeting and exhibit, Reno, NV, January 6–9, 1992
- Thomann H, Frisk B (1967) Measurement of heat transfer with an infrared camera. *Int J Heat Mass Transf* 11:819–826
- Uenal E, Grieb H (2013) stall and transition on elastic rotor blades T1.1 DSA-9A static validation of wind tunnel model. Ferchau engineering report, 2013
- Velkoff HR, Blaser DA, Jones KM (1971) Boundary-layer discontinuity on a helicopter rotor blade in hovering. *J Aircr* 8(2):101–107. doi:[10.2514/3.4423610.2514/3.45910](https://doi.org/10.2514/3.4423610.2514/3.45910)